Contents lists available at ScienceDirect

Journal of Materials Research and Technology

The effects of SLM process parameters on the relative density and hardness of austenitic stainless steel 316L

Mohammadamin Bakhtiarian [a], Hamid Omidvar [a,b,*], Amirhossein Mashhuriazar [a], Zainuddin Sajuri [c], C. Hakan Gur [d]

[a] *Department of Materials and Metallurgical Engineering, Amirkabir University of Technology, Tehran, 1599637111, Iran*
[b] *Center for International Scientific Studies and Collaborations (CISSC) of Iran, Tehran, Iran*
[c] *Department of Mechanical and Manufacturing Engineering, Faculty of Engineering and Built Environment, University Kebangsaan Malaysia, Bangi, 43600, Selangor, Malaysia*
[d] *Department of Metallurgical and Materials Engineering, Middle East Technical University, Ankara, 06800, Turkey*

ARTICLE INFO

ABSTRACT

Selective Laser Melting (SLM) process parameters significantly influence the microstructure and mechanical properties of the final product. Using the Taguchi optimization method, this investigation refined 316L austenitic stainless steel SLM process parameters. Process factors included laser power, scanning speed, and layer thickness, while performance criteria included relative density and hardness. A laser power of 180 W, a scanning speed of 1200 mm/s, and a layer thickness of 0.03 mm produced optimal results, resulting in 125 J/mm^3 energy density and a hardness of 220 HV. ANOVA analysis also showed that power influenced density by 27.49 %, scanning speed by 45.51 %, and layer thickness by 23.60 %. A parameter combination led to materials with impressive tensile strengths (649 ± 4 MPa), yield strengths (409 ± 3 MPa), and elongation (42 ± 1 %) for increasing scanning speed and lowering energy density, resulting in a decrease in ultimate strength. A SEM analysis of fracture characteristics was also conducted. As a result of a cellular microstructure, ductile dimple sizes were limited to the nanoscale, and crack propagation was impeded through a pinning effect, thus increasing defect tolerance in the SLM SS316L. According to the findings, internal defects play a significant role in crack propagation and subsequent reduction of mechanical properties.

1. Introduction

The metal additive manufacturing (AM) industry has evolved significantly due to industrial and societal challenges. Selective laser melting (SLM) stands out among these technologies, although its complexity has posed challenges to the development of new materials due to its complexity. Compared to traditional methods, which typically entail lengthy cycles and high expenses, SLM technology can produce intricate parts more efficiently and at a lower cost than traditional methods [1,2]. The SLM process combines pulsed lasers and powder bed fusion to create complex 3D objects from metallic powders. Due to this technology, it has been possible to produce complex parts with complex geometries, which has resulted in better performance of the parts [3,4].

SLM has many applications that extend beyond the aerospace and automotive sectors [5]. Various approaches have recently been introduced to shape AM components, but SLM has emerged as the most prevalent method [6,7]. An array of components is produced using this process, including components made out of steel, titanium, aluminum, and nickel. As a result of its substantial utility within the biomedical, aerospace, energy, and automotive industries, stainless steel 316L (SS316L) has attracted extensive attention within this context [8–10].

With less than 0.03 % carbon content, SS316L is highly compatible with the SLM process because of its low carbon content [11–13]. While SLM can offer many advantages, it can also cause a wide range of undesirable defects, adversely affecting various properties, including mechanical properties, geometric accuracy, and surface finish on the components produced.

The behavior of SS316L additive manufacturing has been the subject of numerous studies. The study by G. Sander et al. [14] investigated the corrosion properties of 316L stainless steel manufactured through selective laser melting. They observed a direct influence of build orientation on the microstructure of the produced metals and alloys.

Table 1
Chemical composition of the 316L powders Wt. %.

Element	C	Cr	Fe	Mn	Ni	O	P	Si	N	Mo	Cu	Co	Nb	V	N
Wt. %	0.01	17.03	Base	0.59	11.34	0.04	0.2	0.40	0.10	2.51	0.27	0.05	0.02	0.04	0.06

Specifically, specimens built horizontally exhibited larger grains aligned parallel to the build direction. Conversely, smaller and more equiaxed grains were observed in specimens built vertically or at a 45-degree angle. Furthermore, the researchers noted that regardless of the build orientation, specimens fabricated with SLM 316L stainless steel demonstrated higher resistance to pitting corrosion and exhibited a wider passive window compared to their wrought counterparts [14].

Parth Saxena et al. [15] studied the hardness and microstructure of stainless steel 316 using ANOVA analysis methods. Their analysis focused on assessing the impacts of layer thickness and orientation. The results of the ANOVA analysis indicated that lower layer thicknesses led to excellent hardness. This is attributed to the increased ease with which laser sources can melt thin layers of powder particles. The optimal conditions for achieving this were at a 90° orientation and with a layer thickness of 40 μm.

The study conducted by Itziar Tolosa et al. [16] delved into the mechanical characteristics of SS316L steel post-processing via SLM while exploring variations arising from different manufacturing approaches, including alterations in building orientations. Ultimately, these attributes were compared against the established specifications for this steel in its "wrought" form. Notably, the yield strengths of this alloy were found to be more significant following the SLM process compared to its rolled state. Furthermore, it was observed that SLM specimens exhibited a hardness akin to what is seen in wrought products of this alloy. Charpy test results suggested that these specimens had a marginally lower value than wrought products' specifications.

The investigations led by Tomasz Kurzynowski et al. [17] have revealed that laser power and scanning methods significantly influence the microstructures and textures of materials. Their findings indicate that laser energy density and scanning strategy play a crucial role in shaping the cellular substructure of austenite, determining the presence of ferrite, and influencing the type and intensity of texture. This culminated in a twofold increase in yield strength, enhanced ultimate tensile strength, and a 1.4-fold reduction in elongation at fracture compared to hot-rolled SS316L sheets.

In a study conducted by Jin Myoung Jeon et al. [18], the impact of microstructure and internal defects on the mechanical behavior of austenitic stainless steel 316L produced through selective laser melting was examined. The research revealed that the presence of pores predominantly influenced the anisotropy observed in tensile tests. Due to localized stress concentrations around these pores, it led to localized yielding and subsequent crack propagation. This, in turn, resulted in significant disparities in strength and ductility.

In recent years, numerous studies have investigated printing defects, such as porosity, keyhole formation, balling, and melt pool stability [19–24]. In order to minimize defects in SLM, it is crucial to understand a range of processing parameters, such as layer thickness, scanning strategy, pattern filling distance, spot size, focus, and laser power, that are crucial to the process [25].

Pore formation, for instance, is attributed to improper selection of laser power and scan speed [26]. Larimian et al. [27] demonstrated that higher laser power and slower scanning speeds significantly enhance the mechanical properties of SLM-processed samples. Laser power exerts a more significant influence on SLM processes than scanning speed. Hsu et al. [28] noted that low laser power prevents 316L powder from melting and bonding, while high power leads to keyhole formation.

Short hatch spaces resulted in the highest density and hardness for 316L. Conversely, long hatch spaces yielded the lowest relative density for the samples. Achieving effective powder layer fusion necessitated higher energy density as hatch space increased. Ronneberg et al. [23]

Table 2
Specifications of the NOURA M100P SLM machine.

Building Volume, (**mm × mm**)	**Ø125 mm × 150 mm height**
Layer Thickness, (μm)	20–80
Laser System, (W)	Fiber laser 300
Optic System, (−)	F-theta-lens; High-speed scanner
Scanning Speed, (m/s)	Up to 7.0
Focus Diameter, (μm)	Approx. 80
Production Speed, (cm³/h)	Up to 20
Inert Gas, (−)	Nitrogen or Argon

Table 3
The Design of Experiments' parameters and levels.

Sample	Power (W)	Scanning Speed (mm/s)	Layer Thickness (μm)	Volumetric Energy Density (VED) (j/mm³)
C-1	150	800	30	156
C-2	150	1200	40	78
C-3	150	1600	50	46
C-4	150	2000	60	31
C-5	180	800	40	140
C-6	180	1200	30	125
C-7	180	1600	60	46
C-8	180	2000	50	45
C-9	210	800	50	131
C-10	210	1200	60	72
C-11	210	1600	30	109
C-12	210	2000	40	65
C-13	240	800	60	125
C-14	240	1200	50	100
C-15	240	1600	40	93
C-16	240	2000	30	100

observed a positive and directionally dependent correlation between porosity and ductility. Horizontally constructed samples exhibited higher porosity levels but more excellent ductility, a phenomenon explained by the shape and orientation of pores. Most porosity stemmed from significant fusion defects and pores with a high aspect ratio clustered along layer boundaries. Pore accumulation was evident on the fracture surfaces of both horizontal and vertical samples.

A study on the effects of laser power, scanning speed, and layer thickness on the microstructure, density, and hardness of austenitic stainless steel 316L has been conducted in this study. This study's novelty lies in assessing the effects of the SLM process's laser power, scanning speed, and layer thickness on the metallurgical and mechanical properties of stainless steel 316L. The selected specimens were evaluated as part of the metallographic and mechanical investigations. The Taguchi and ANOVA methods were used to test the effects of each parameter on the selected specimens. This work will likely lead to the developing of a standard SLM method that can be used in various industries due to its success.

2. Materials and experimentation

2.1. Experimental materials and parameter setting

This study utilized AISI 316L stainless steel powder, which was atomized using N_2 gas. The procurement of this powder was carried out through VISTEC TECHNOLOGY SERVICES, Inc. The composition of the 316L stainless steel powder was determined using Spark Emission

Table 4
The process parameters.

Level	Scanning Speed (mm/s)	Power (W)	Layer thickness (mm)	Hatch space (mm)	VED (J/mm^3)
1	1100	180	0.03	0.04	136
2	1200	180	0.03	0.04	125
3	1300	180	0.03	0.04	115

Spectroscopy with an OXFORD device, following the reference standard ASTM E1010-16. Detailed information regarding the chemical composition of the 316L powders can be found in Table 1.

Utilizing a NOURA M100P SLM machine, a series of 316L stainless steel cuboid parts, each measuring 10 × 10 × 10 mm, were fabricated. The specifications of this machine are outlined in Table 2.

The study employed the Design of Experiments (DOE) approach to optimize process parameters. Three critical parameters in 3D printing via SLM were identified: laser power, scan speed, and layer thickness. The DOE was structured using Taguchi's L16 orthogonal arrays, encompassing three parameters and four levels. All parameters were set at four levels to enhance SLM's overall production efficiency. The hatching space (h) was maintained at 0.04 mm. An overview of the process parameters and their respective values is provided in Table 3.

In order to evaluate the effect of scanning speed on the mechanical properties, a narrower range of scanning speeds was used to make tensile samples. According to Table 4, this selection aimed to examine the effects of speed on mechanical properties within an optimal parameter range.

The choice of scanning speeds (1100 mm/s, 1200 mm/s, and 1300 mm/s) was determined to encompass the critical variations observed in the density cube results. These speeds were selected based on their alignment with the optimal range identified in the preliminary analysis. Regarding the laser power and layer thickness for preparing the tensile samples, the laser power used was 180 W, and the layer thickness employed during sample fabrication was 0.03 mm.

Additionally, horizontal printing was favored due to its reported higher tensile strength, according to established research [14,29,30]. The manufacturing process involved producing three blocks following the parameters outlined in Table 4. Subsequently, sub-size samples were extracted from these blocks using EDM wire cutting. This method minimizes material damage and ensures conformity with ASTM E8M standards for specimen dimensions.

2.2. Characterization methods

A scanning electron microscope (SEM) was utilized to examine the powder's structure. The particle size distribution of 316L powder was assessed using a Bettersizer 2600 instrument. The powder's Apparent Density (AD) and Tap Density (TD) were evaluated utilizing a Hall Flowmeter Funnel following ASTM B213 and ASTM B212 standards.

Furthermore, the powder's flow ability was gauged through the Hausner Ratio (AD/TD). The cubic samples were meticulously smoothed with sandpaper post-separation to enhance the precision of density measurements. Springs et al. [31] deduced that the Archimedes method is the most accurate and efficient approach for determining the density of waterproof samples generated through additive manufacturing. Consequently, cube density was ascertained using the Archimedes method as per ASTM B962.

An electronic scale with a precision of 0.001 g was employed to weigh the samples. Each sample underwent five measurements, and prior to each reading, it was thoroughly dried.

The phase compositions of the samples were analyzed via X-ray Diffraction (XRD) using an EQUINOX3000 instrument. The surface of the selected sample for XRD testing was meticulously polished to a smooth 1 cm^2 size. The analysis encompassed a scanning range of $2\theta = 30°–100°$, a step size of $0.02°$, and a scanning speed of $5°$/min. Subsequently, the samples were cross-sectioned perpendicular to the surface following the XRD analysis. Following further refinement with abrasive paper, the parts were polished using a polishing machine. In the subsequent step, the polished samples underwent a 15-s etching process with an aqua regia solution (1:3 nitric acid/hydrochloric acid).

An Optical Microscope (OM, OLYMPUS U-SWTR-3) and a Scanning Electron Microscope (SEM) were used to observe the microstructure and cellular grain structure.

In order to evaluate the material's strength in relation to the SLM device that was used, tensile testing was conducted on a Universal Testing Machine in accordance with ISO 6892-1. The test specimens were manufactured horizontally [29]. Before the tests, the surfaces of the specimens were ground to remove high-stress concentration zones that may cause premature failure during the test. A constant speed of 0.5 mm per minute was used to test the specimens until rupture had been achieved. An extensometer measured the elongation of the tensile specimens during testing, and a 10 KN load cell was used to determine the applied force.

Vickers hardness on the cross sections (XY plane) was measured using a Mitutoyo HM-211 microhardness tester (Mitutoyo Co., Japan) with a 20-s indentation. Mechanical tests were carried out under consistent conditions, with a minimum of three repetitions, and the mean value was computed. Additionally, SEM was utilized to inspect the fracture surfaces of the tensile specimens.

3. Results and discussion

3.1. Characterization of 316L powder feedstock

Fig. 1(a) depicts the morphology of the 316L powder utilized in this study. The gas-atomized 316L powder exhibits spherical particles with satellite formations. Smaller ones occasionally aggregate on the surface
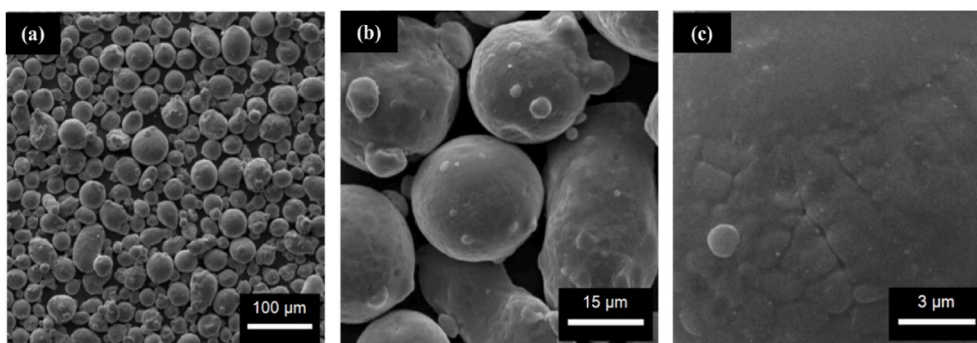

Fig. 1. Various scanning electron microscope (SEM) images of 316L powder used in this study are presented, showing its morphology at different magnifications: (a) at 200 μm, (b) at 20 μm, and (c) at 5 μm.
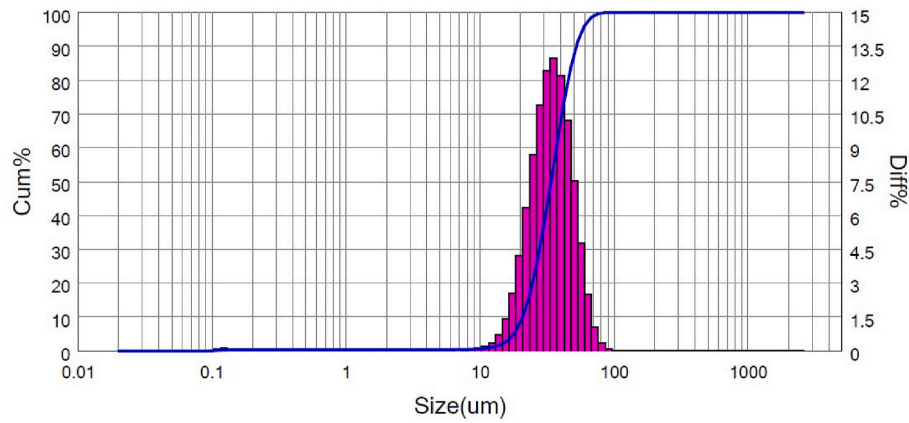
Fig. 2. Distribution of particle diameters.

Table 5
Physical properties of SS316L powder.

Particle Size Distribution (μm)			Apparent Density (g/cc)	Tap Density (g/cc)	Hausner Ratio (AD/TD)	Fluidity (s/50g)
D10	D50	D90	4.25	4.79	1.12	16.77
20.78	33.81	51.84				

of larger powder particles, as illustrated in Fig. 1(b).

Satellites form due to tiny powder particles adhering to larger ones during gas atomization. This phenomenon arises from disparities in flow conditions, crystallization rates, and interactions between liquid and solid steel droplets [2]. As shown in Fig. 1(c), the powder surface predominantly displays a smooth texture, indicating a blend of solidification structure and imperfections in solidification. Surface irregularities and occasional occurrences of smaller spheres signify these imperfections. While these defects may lead to an increase in surface roughness, they are not anticipated to have a significant impact on the SLM fabrication process [29].

Based on the results obtained from the particle size analyzer Bettersizer 2600, Fig. 2 presents the normal histogram illustrating the particle size distribution.

In addition, Table 5 provides particle size distributions, apparent densities, tap densities, fluidities, and Hausner ratios for the 316L powder. The average particle size of the 316L powder measured 33.81 μm.

A notable proportion of the particles fell below 52 μm in size. The Hausner ratio for the 316L powder was determined to be 1.12. A Hausner ratio exceeding 1.25 indicates relatively subpar flow ability.

This is primarily attributed to the propensity of smaller particles to interlock with larger ones, leading to heightened friction among particles and hindering powder mobility [32].

The powder demonstrated a flow duration of 13.93 s during the Hall-flow test, exhibiting impressive flow ability due to its spherical form and the existence of small satellites. The powder flowed smoothly when dispersed thinly without agglomeration within the SLM machine.

3.2. Density and hardness

The relative density and hardness of each sample were evaluated as response variables. The average values for these response variables are outlined in Table 6. Among the 16 samples, four exhibited relative densities surpassing 98 %.

Sample C-4 demonstrated the lowest relative density, attributed to utilizing the lowest laser power at 150 W, the highest scan speed of 2000 mm/s, and the thickest layer measuring 0.06 mm. Figure 3 shows that process factors have a significant influence on relative density. Porosity is significantly affected by factors related to energy density, including laser power, scanning speed, hatch spacing, and layer thickness [33–35]. This influence arises from their impact on the temperature profile and liquid/gas flow dynamics within the processing area. Mathematically, relative density is defined as:

$$VED = P/(V \times H \times L) \tag{1}$$

Among these, P represents laser power, V indicates scan speed, L indicates layer thickness, and H indicates hatch spacing. According to Fig. 3, there are optimal laser power values for SLM of 316L that minimize porosity [36]. Low laser power or high scanning speed combined with thick layers (resulting in low energy density) can form irregular
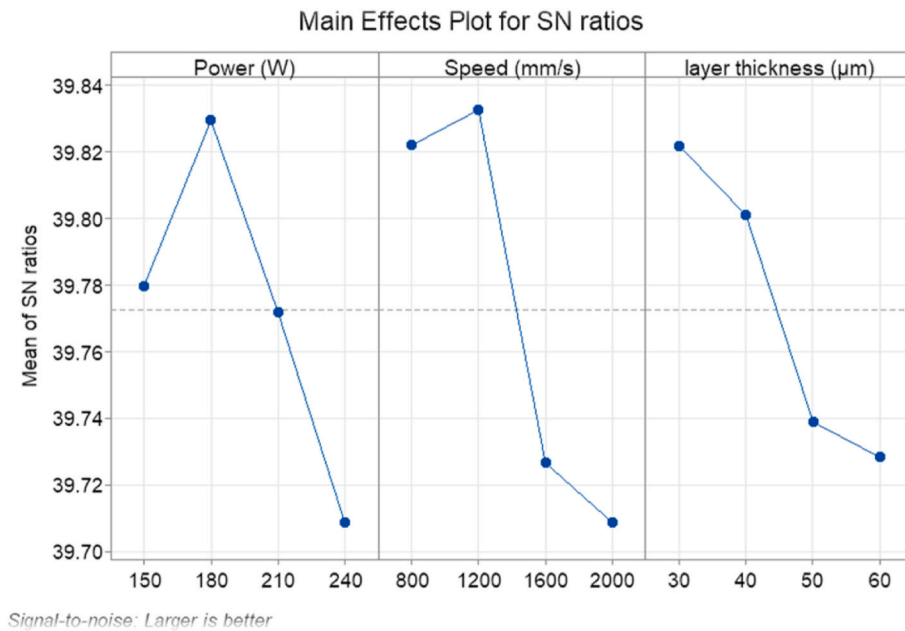
Table 6
Results of SLM experiment.

Exp. No.	Power (W)	Scanning Speed (mm/s)	Layer Thickness (μm)	VED (j/mm^3)	Density (%)	Hardness (HV)
C-1	150	800	30	156	98.60	210
C-2	150	1200	40	78	98.20	205
C-3	150	1600	50	46	96.70	189
C-4	150	2000	60	31	96.30	179
C-5	180	800	40	140	99.05	207
C-6	180	1200	30	125	99.50	220
C-7	180	1600	60	46	96.80	190
C-8	180	2000	50	45	96.90	190
C-9	210	800	50	131	97.65	199
C-10	210	1200	60	72	97.78	195
C-11	210	1600	30	109	97.30	192
C-12	210	2000	40	65	96.90	187
C-13	240	800	60	125	96.60	191
C-14	240	1200	50	100	96.90	188
C-15	240	1600	40	93	96.80	186
C-16	240	2000	30	100	96.50	180

Fig. 3. Relationship between process parameters and relative density.

Table 7
Analysis of Variance for density.

Source	DF	Adj SS	%	Adj MS	F-Value	P-Value
Power (W)	3	3.7510	27.49	1.2503	16.19	0.003
Scanning Speed (mm/s)	3	6.2097	45.51	2.0699	26.80	0.001
Layer Thickness (µm)	3	3.2207	23.60	1.0734	13.90	0.004
Error	6	0.4634	3.40	0.0771	–	–
Total	15	13.6445	100.00	–	–	–

pores or crevices due to balling and inadequate melting [37].

Conversely, with high laser power and low scanning speed (resulting in high-energy density), spherical pores were observed, attributed to material evaporation and the entrapment of inert gases during solidification [38]. Furthermore, porosity tends to escalate with the increase in powder layer thickness [39].

As indicated in Table 7, power affects density by 27.49 %, scanning speed by 45.51 %, and layer thickness by 23.60 %. This table demonstrates that all factors have a substantial impact on density. In the ANOVA results, Scanning Speed exhibited a significantly higher significance level than Layer Thickness, and power held a relatively lower significance level. This conclusion aligns closely with the findings of Aniket K. Dutt et al. [40].

To evaluate how the process parameters affect sample density, variance analysis (ANOVA) was employed. The ANOVA results for all
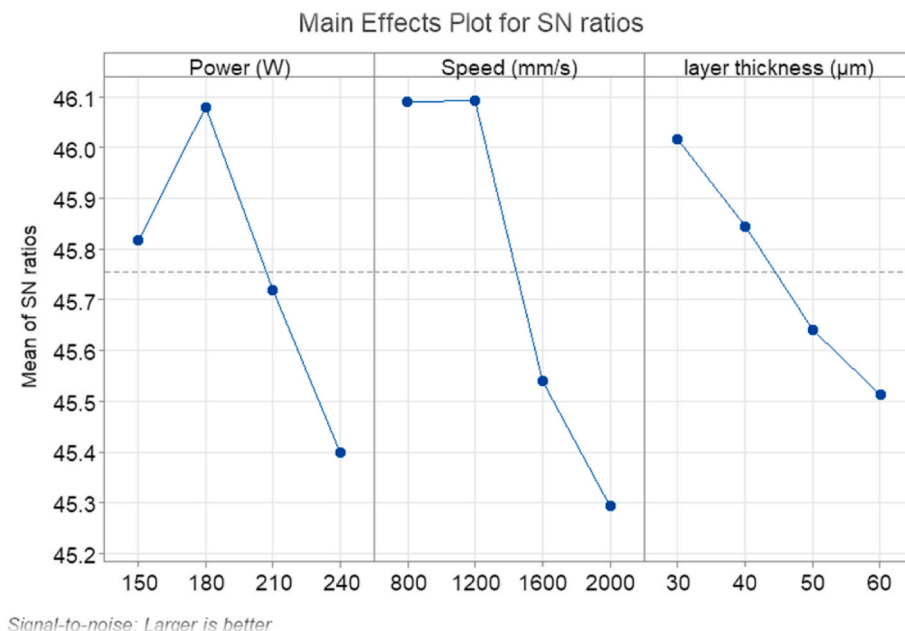

Fig. 4. The effect of process parameters on hardness.

Table 8
Analysis of Variance for hardness.

Source	DF	Adj SS	%	Adj MS	F-Value	P-Value
Power (W)	3	494.00	26.17	164.67	11.76	0.006
Scanning Speed (mm/s)	3	985.50	53.24	328.50	23.46	0.001
Layer Thickness (μm)	3	323.50	17.14	107.83	7.70	0.018
Error	6	84.00	4.45	14.00	–	–
Total	15	1887.00	100.00	–	–	–

outcomes are detailed in Table 7, along with corresponding F- and P-values for individual process parameters and their interactions.

A process parameter with a high F-value and a P-value below 0.05 (indicating 95 % confidence) significantly influences density. P-values signify the likelihood of a specific outcome occurring by chance, while F-values denote a relatively more significant variance among groups. For a statistical test to be considered meaningful, P-values must be less than 0.05 [41,42].

As depicted in Fig. 4, each parameter—power, scanning speed, and layer thickness—influences hardness. Initially, the hardness of a material increases with higher power settings but eventually decreases with further power increases.

Conversely, higher speed and thickness settings tend to reduce hardness. Both Figs. 3 and 4 affirm a correlation between density and hardness values. The hardness of additively manufactured parts is influenced by microstructure and powder melting.

Studies by Wakshum M. Tucho [11] and Hua-Zhen Jiang [43] have established that porosity significantly affects material hardness. The hardness of an additively manufactured component will vary depending on its microstructure and the degree of powder melting. If there is insufficient powder melting and a prevalence of pores, the hardness of the fabricated part may not reach its full potential [40]. The relationship between density and hardness is evident in Table 6, demonstrating a hardness decrease at both high and low energy densities. These findings align with those of Cherry et al. [44].

The highest recorded hardness in this study was 220 HV. An analysis of variance (ANOVA) was conducted to determine the influence of each process parameter on the hardness of each sample. Table 8 provides the F- and P-values for individual process parameters and their interactions for all the outcomes, as mentioned earlier. It is evident from Table 8 that power influences hardness by 26.17 %, scanning speed by 53.24 %, and layer thickness by 17.14 %. Notably, a built part's porosity and microstructure significantly impact its hardness. Scanning speed has a more significant effect on hardness than power, while power exerts a more significant influence than layer thickness.

3.3. Characterization of SLM 316L parts

Fig. 5 illustrates the XRD patterns of the precursor powder and the SS316L samples fabricated at two distinct Volumetric Energy Density (VED) values, 31 and 156 J/mm^3. Neither the powder nor the solid samples exhibited any indications of ferrite presence. These findings align with those reported by Sijia Liu [45].

No distinct preference for specific crystallographic orientations is observed in the Selective Laser Melting (SLM) context. In contrast to the precursor powder, the as-built sample exhibits broad peaks resulting from residual stresses and dislocations introduced during the SLM process [46].

In the context of Selective Laser Melting (SLM), no distinct preference for specific crystallographic orientations is observed. In contrast to the precursor powder, the as-built sample exhibits broad peaks, a result of residual stresses and dislocations introduced during the SLM process [47,48].

Also, it can be seen In XRD patterns that an upward shift in Bragg angles within the manufactured samples and correlates with increased energy density. This phenomenon suggests a possible lattice distortion induced by laser-induced thermal stress [44]. As indicated by Mostafa Yakout et al. [49], there is a notable increase in both horizontal and vertical stresses with rising laser energy density. This increase in energy density is known to escalate thermal stress levels, resulting in a higher temperature gradient, ultimately leading to more significant thermal stress within the material. The observed trend of upward-shifted Bragg
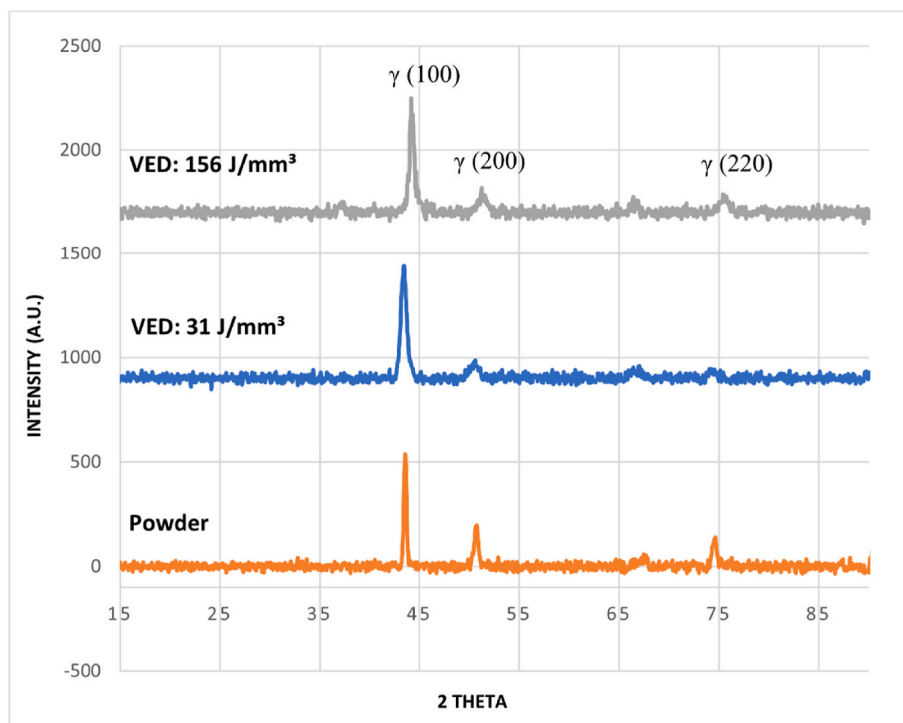

Fig. 5. XRD pattern of the powder and parts of 316L processed by SLM under different VED.
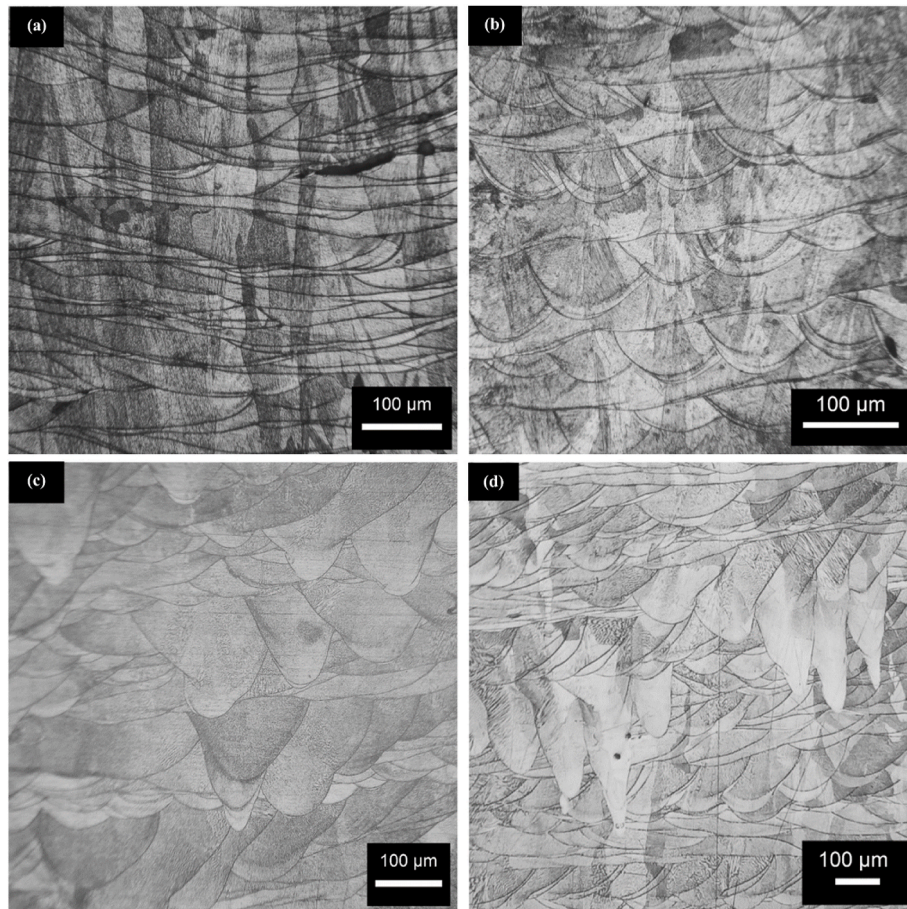
Fig. 6. – Optical micrographs specimen (a) C-3 at VED of 46 J/mm^3, (b) C-9 at VED of 131 J/mm^3, (c) C-5 at VED of 140 J/mm^3, and (d) C-1 at VED of 156 J/mm^3, in xz-plane.

angles aligns with this understanding. As energy density rises, the amplified thermal stress likely induces lattice distortion, contributing to the observed shift in Bragg angles.

3.4. Microstructure of SLM 316L parts

The SLM SS316L sample C-6, as detailed in Table 6 has undergone microstructural analysis using optical microscopy (OM), revealing distinct hierarchies at the macro, micro, and nanoscale levels in its as-built state. Layered microstructures with clearly defined melt pools are discernible at the macro level. The optical micrographs indicate complete melting of the powder, and the melt pools in vertical planes exhibit a characteristic 'fish scale' morphology (Fig. 6(a)). Fig. 6(b) displays the melting traces and melt pools generated by the scanning laser beam. In sample C-6, the melt pool width measures approximately 130 μm, while the height is about 60 μm, depending on the direction of the laser beam. The melt pool size may vary based on laser spot size and input energy density [46].

With each repetition, previously heated melt pools can undergo partial re-melting, resulting in well-aligned melt pools spaced regularly. The boundaries of melt pools may have different separations due to localized inhomogeneities within them [50]. A decision was made to measure the depth of melt pool boundaries on a cross-section parallel to the build direction (xz) to compare melt pools in parts manufactured with different Volumetric Energy Densities (VEDs). According to Fig. 6, the size of the molten pool changes as the VED changes. Fig. 6(a) il-lustrates that with a VED of 46 J/mm^3, the melt pool is shallow, with an average depth of around 30 μm. On the other hand, Fig. 6(b)–6(d) illustrate that with a VED of 131 J/mm^3 to 156 J/mm^3, the average melt
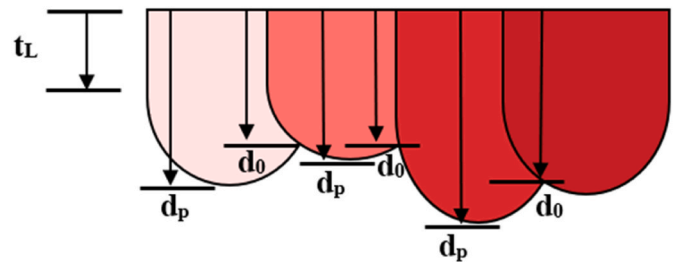

Fig. 7. – Schematics of top layer melt pool measurements on X-Z cross-section.

pool depth increases to 60 μm, 90 μm, and less than 120 μm, respectively.

As shown in Fig. 7, the d_p/t_L value represents the depth of a melt pool relative to the nominal layer thickness. In contrast, the d_0/t_L value represents the depth of an overlapped melt pool relative to the nominal layer thickness. Table 9 provides measurements for various VEDs.

This measurement aims to illustrate how melt pools, or more

Table 9
The d_p/t_L and d_0/t_L of melt pool boundaries measured at different VEDs.

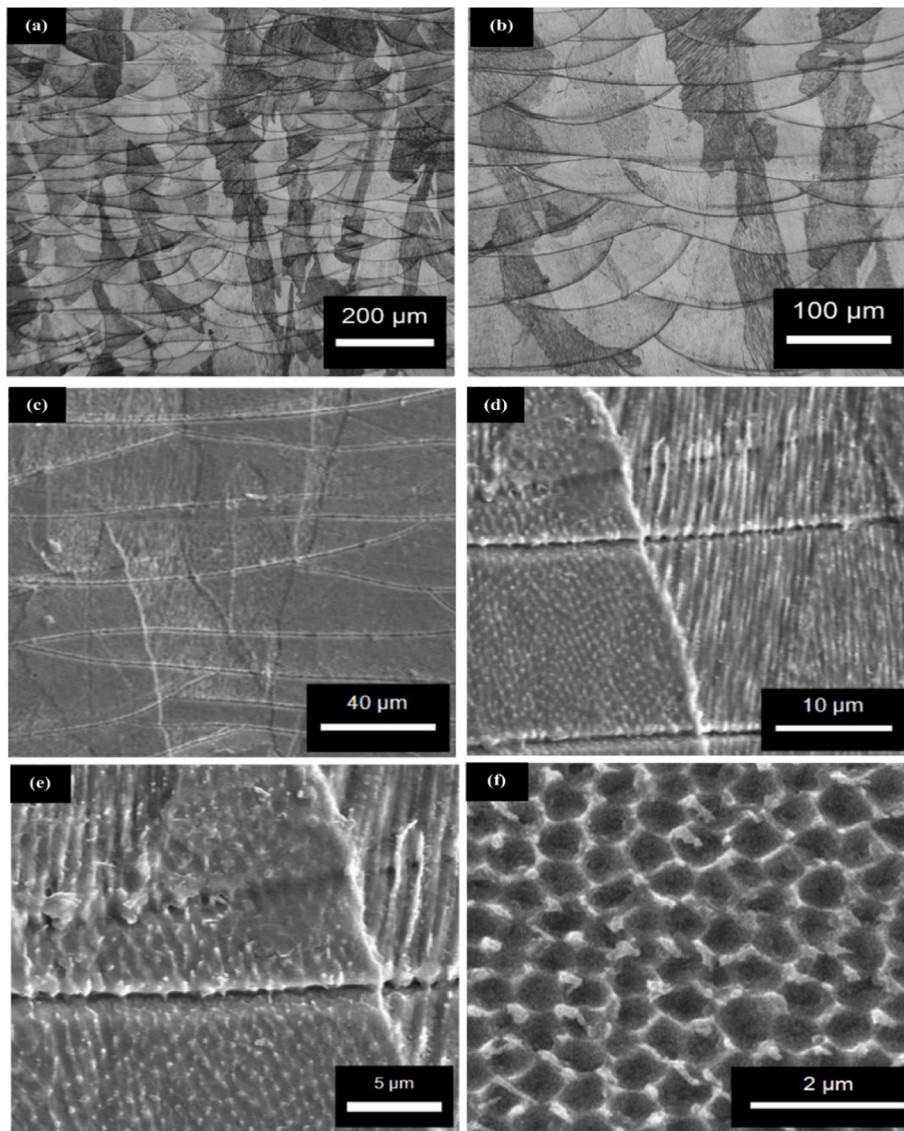| VED (j/mm^3)	d_p/t_L	d_0/t_L
156	9.04 ± 0.02	7.22 ± 0.12
140	6.55 ± 0.62	3.22 ± 0.13
136	3.36 ± 0.13	2.12 ± 0.34
78	2.05 ± 0.24	1.82 ± 0.85
46	1.78 ± 0.05	1.19 ± 0.56

Fig. 8. – Optical micrographs and SEM micrographs specimen C-6 in xz-plane.

precisely melt volumes, impact the density of parts fabricated by SLM under different VED conditions. A VED of 156 J/mm^3 resulted in melt pool boundaries with d_p/t_L of 9.04 and d_0/t_L of 7.22. When the VED was 46 J/mm^3, these values were 1.78 and 1.19, respectively. According to equation (1), melt pool volume is directly proportional to VED and inversely proportional to scanning speed. Increasing VED values promotes densification by melting and filling porosity [35].

In Fig. 8 (a) and (b), optical microscopy (OM) images vividly depict large columnar grains within the melt pools. These columnar grains become distinctly visible upon etching, ranging from several tens of microns to as much as 100 μm. The temperature gradient determines the growth of these columnar grains they experience [29]. As observed in Fig. 8 (c) and (d), it is apparent that columnar grains may extend across the melt pool boundary, as the laser consistently exposes the top surface of the solid part [51]. The molten powder and previously solidified layer must be coherent in terms of chemistry and crystallography in order to allow these grains to persist. As long as voids, porosity, or balling effects did not introduce chemical or crystallographic composition variations, the nucleation of new grains was unimpeded. Due to these congruities, the grains grew in alignment with the crystal orientation of the preceding layer [44,52]. Molten material solidifying in its preferred orientation at high volumetric energy density (VED) has an extended

solidification period due to the substantial thermal gradient. Consequently, increasing VED leads to an enlargement in columnar grain size [35]. It is confirmed in the study by Larimian et al. [53] that grain size increases with increasing energy density. They also provided an explanation for this phenomenon, highlighting that higher energy density leads to larger melt pools. These larger melt pools consequently lead to a coarser microstructure.

At the micro level, a distinctive cellular segregation network structure is prominently observed, as depicted in Fig. 8 (d), (e), and (f). A columnar grain encompasses this cellular structure, with cells ranging between 0.5 and 1 μm in diameter. Recent studies have demonstrated that neighboring cells exhibit similar crystallographic orientations, suggesting that this structure deviates from the typical characteristics of grain boundaries. The high cooling rates experienced during the SLM process give rise to this cellular structure due to non-equilibrium conditions [54,55].

Fig. 8 (d) illustrates that this cellular structure can manifest either in an equiaxed or bar-like configuration, contingent on the growth direction of its larger columnar grains. The high-magnification SEM image in Fig. 8 (d) vividly showcases the three-dimensional morphology of the cellular structure along the longitudinal direction, revealing square, pentagon, and hexagon shapes in the transverse direction [56].
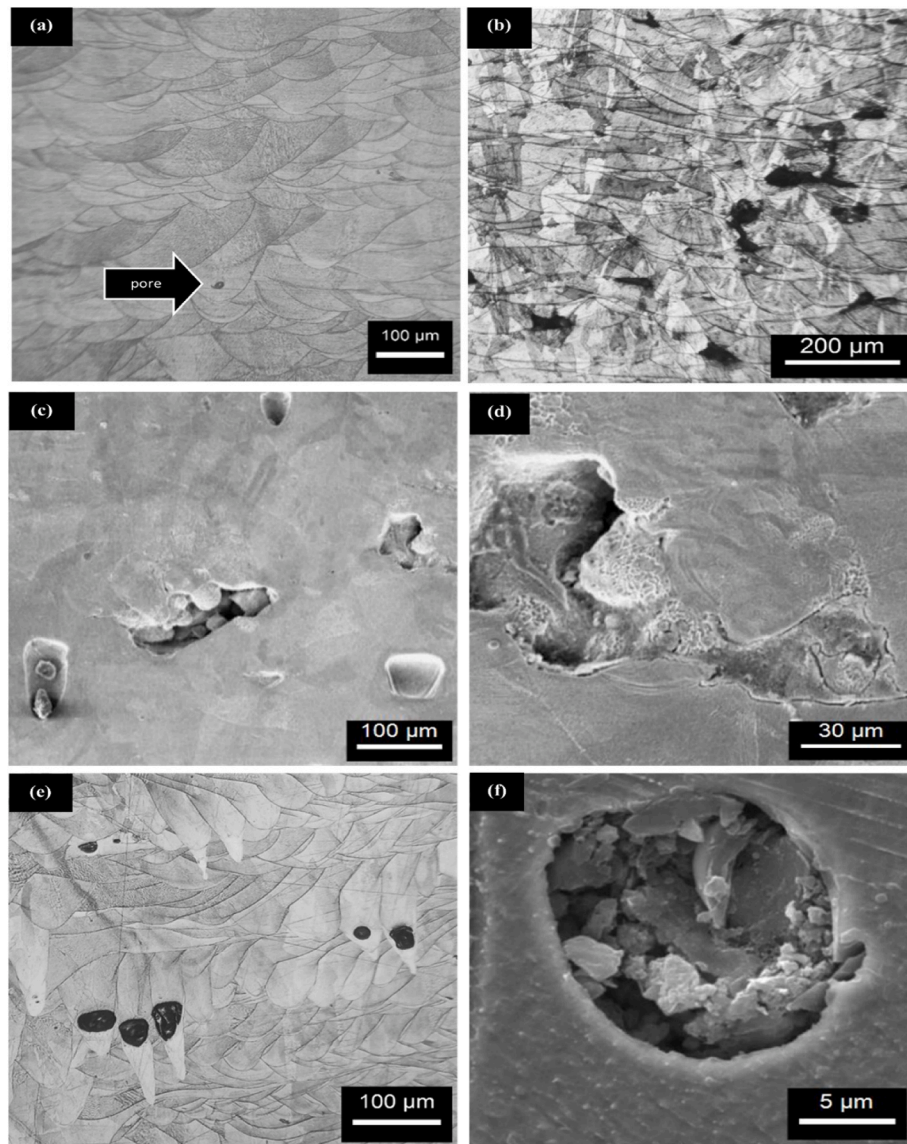
Fig. 9. Optical micrographs specimen (a) C-6 at VED of 125 J/mm^3, (b) C-4 at VED of 31 J/mm^3 and (e) C-1 at VED of 156 J/mm^3, SEM micrographs specimen (c and d) C-4 at VED of 31 J/mm^3 and (f) C-1 at VED of 156 J/mm^3, in xz-plane.

In response to laser scanning, particularly the temperature gradient, the cellular structure predominantly aligns along the building direction, with its longitudinal direction parallel to the building direction [47]. These cellular structures accumulate dislocations and residual stresses due to segregating heavy alloying elements such as Mo and Cr. The SLM process typically involves rapid melting and solidification far from equilibrium [51].

3.5. Defects

Optical and scanning electron microscopy were used to examine the solidification defects in SS316L-SLM samples. Substrate porosity is significantly influenced by parameters associated with energy density, including laser power, scanning speed, hatch spacing, and layer thickness. These parameters substantially impact the temperature evolution and flow dynamics within the processed area [39].

To minimize porosity in SS316L-SLM, adjustments to laser power and scanning speed are crucial. Fig. 9(a) displays a perpendicular cross-section of sample C-6, exhibiting a density of 99.5 % and a Volumetric Energy Density (VED) of 125 J/mm^3.

The micrographs in Fig. 9 (b), (c), and (d) showcase perpendicular cross-sections of sample C-4, characterized by the lowest VED and density at 96.30 %. Lastly, Fig. 9 (e) and (f) present SEM images of the sample with the highest VED of 156 J/mm^3, resulting in a density of 98.60 %.

Fig. 9 (a) depicts that the sample with the highest density exhibits a few minor pores. Notably, there were no cracks or substantial porosities observed between the layers. Additionally, tiny pores were identified at the center of the melt pool, where temperatures peaked.

According to Tables 1 and it is evident that the 316L powder contains 0.1 wt % nitrogen, a byproduct of its gas atomization production process. The formation of tiny, spherical pores during solidification results from gas entrapment and nitrogen absorption.

The research done by Bose et al. [57] and Milad Ghayoor et al. [35] confirmed the impact of nitrogen content on porosity during the SLM process. Bose et al. investigated two distinct powder mixtures containing 0.065 mass-% and 0.27 mass-% nitrogen content in the 316L alloy samples produced via selective melting by laser in the SLM process. These variations in nitrogen content within the powder mixtures resulted in observed specimen porosity ranging from 0.17 % to 0.91 %.

Their research highlighted that nitrogen outgassing from the melt during solidification significantly impacted specimen density during

Table 10
Mechanical properties of SLM SS316L and reference.

Material	Scanning Speed (mm/s)	VED (J/mm3)	Yield Stress (MPa)	UTS (MPa)	Elongation (%)
1	1100	136	372 ± 6	624 ± 8	50 ± 4
2	1200	125	380 ± 6	640 ± 6	52 ± 1
3	1300	115	409 ± 3	649 ± 4	42 ± 1
Reference	N/A	N/A	170	485	40

SLM processing. Specifically, the nitrogen content in SLM-built specimens was found to be contingent upon the maximum solubility of the liquid phase. Outgassing occurred if this solubility limit was surpassed, leading to lower specimen density. Conversely, if nitrogen remained below the maximum solubility, the steel absorbed nitrogen from the process atmosphere.

Additionally, Milad Ghayoor's [35], study on selective laser melting of 304L provided complementary insights, attributing minor spherical porosity in SLM to gas entrapment within the powder feedstock and nitrogen gas absorption during solidification. These observations align with Bose et al.'s findings on nitrogen's impact on specimen density during the solidification phase in SLM processes.

These observations reinforce the critical role of nitrogen content and its interaction with the SLM process, substantiating the link between nitrogen, porosity variation, and outgassing during solidification in additive manufacturing processes like SLM.

Microstructure images of the sample with the lowest Volumetric Energy Density (VED) of 31 J/mm^3 (achieved with 150 W, 2000 mm/s scanning speeds, and 0.06 mm layer thickness) displayed in Fig. 9 (b), (c), and (d) vividly illustrate that the voids exhibit irregular shapes and sizes. There are also irregular cavities along the borders of melt pools, indicating incomplete fusion [58]. Small triangular voids may form at the intersection of three melt pools if the top two melt pools fail to melt the bottom layer fully. Pores with irregular shapes and sizes are primarily near fusion lines, suggesting inadequate energy density. Additionally, due to the propensity of austenitic stainless steel to develop

porosity when exposed to argon gas, gas holes induced by this gas are noticeable in the microstructure of these samples [59–61].

In Fig. 9(e), the microstructure of a sample subjected to the highest Volumetric Energy Density (VED) (150 W power, 800 mm/s scanning speed, and 0.03 mm layer thickness) is depicted. Neither the powder bed nor the powder itself appear to have entrapped gas. At this elevated level of VED, which creates intense thermal conditions, powder particles undergo melting both within and between layers.

With increased VED, molten pools develop keyhole cavities due to the growing ratio between their depth and width [62]. Fig. 9(e) provides an electron microscope image of a keyhole. When high laser energy is applied to a melt pool, gas bubbles form, resulting in near-spherical defects ranging from 40 to 70 μm. Due to the keyhole effect, low melting point constituents in the alloy may vaporize and accumulate gas bubbles in the melt pools. The downward conduction of thermal energy during solidification gives rise to temperature gradients. It is important to note that these gas bubbles form well below the surface of the melt pool. Due to the high solidification rate, gas bubbles cannot escape from the surface of the melt pool [63–66].

3.6. Mechanical properties

Components produced through Selective Laser Melting (SLM) were tested using the parameters outlined in Table 10. Subsequently, a comparison was made between these results and those obtained from conventionally annealed bars, evaluating the efficacy of the two methods.

The engineering stress-strain curves of SLM 316L are presented in Fig. 10 for scanning speeds of 1100 mm/s, 1200 mm/s, and 1300 mm/s.

Furthermore, these values were juxtaposed with those for wrought 316L Stainless Steel, which possesses yield strengths of 170 MPa and ultimate tensile strengths of 485 MPa. Notably, the stress-strain curve lacks a distinct yield stage for yield strength, as illustrated in Fig. 10. The yield strength ranges from 372 ± 6 MPa to 409 ± 3 MPa at a 0.2 % strain.

The relationship between the yield strength of 3D printed components and scanning speed has been closely examined in the study conducted by Jiangwei Liu [67]. The ultimate tensile strength (UTS) slightly decreased with increasing energy density, reaching a maximum of 649
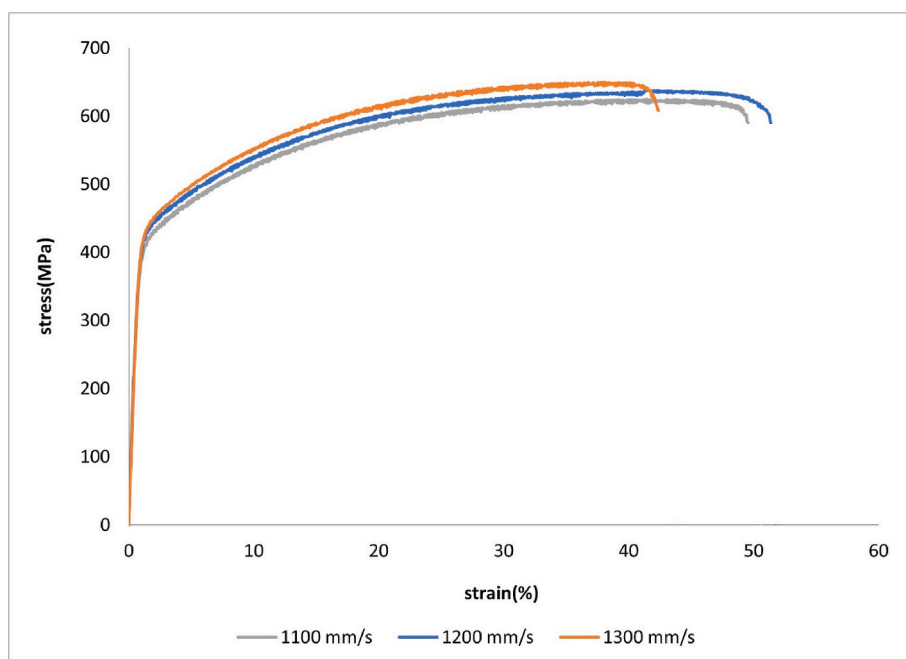
Fig. 10. Stress strain curve for SLM 316L at scanning speeds of 1100 mm/s, 1200 mm/s, and 1300 mm/s.
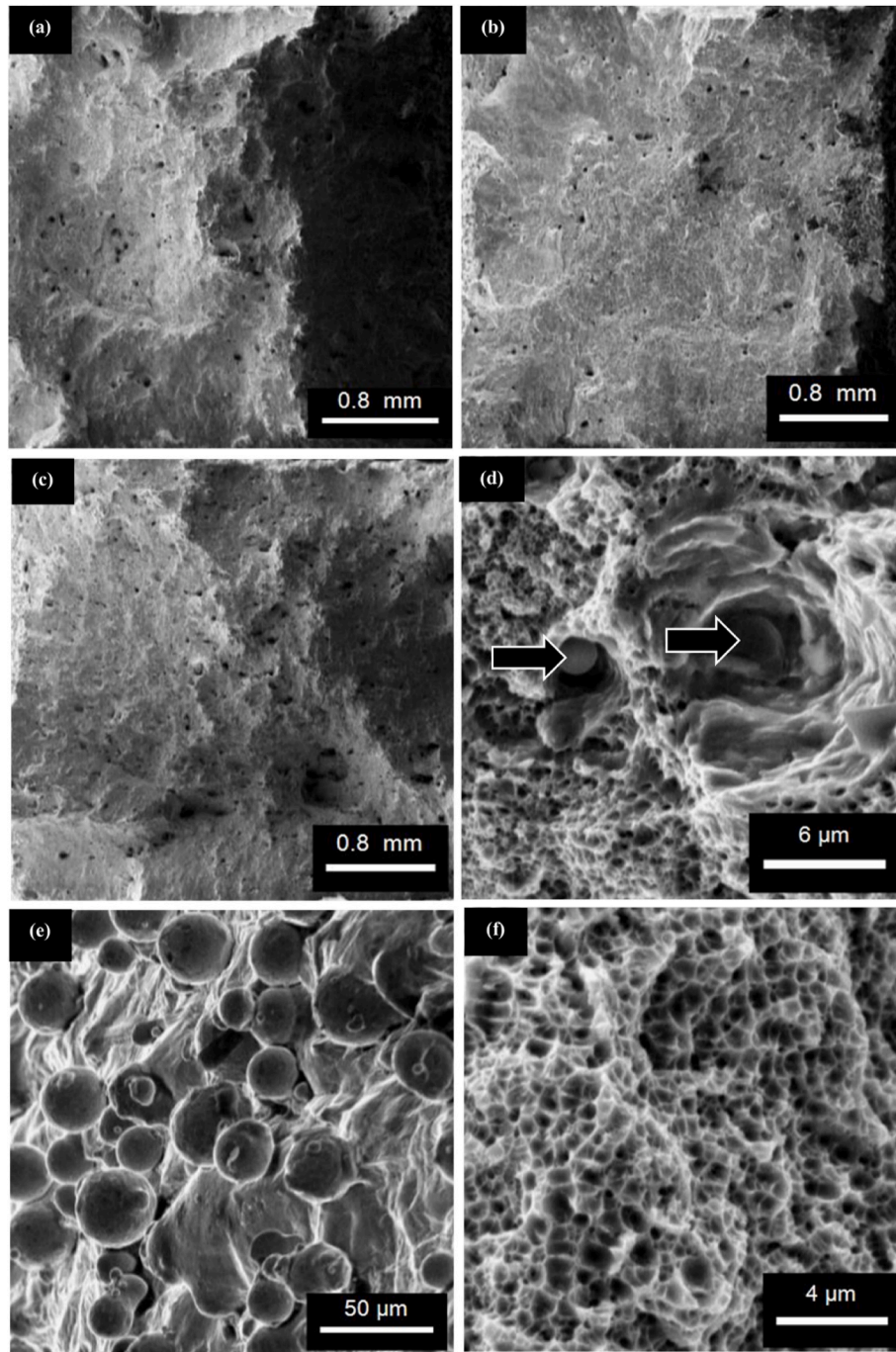
Fig. 11. Fractography of tensile specimens of SLM SS316L at three different scanning speeds: (a) 1100 mm/s (b), 1200 mm/s, and (c) 1300 mm/s (e), (d) and (f) high magnification images of tensile specimens' fractured surfaces.

± 4 MPa at a scanning speed of 1300 mm/s (refer to Table 10). On the other hand, with rising input energy, there was a slight increase in elongation to failure (see Fig. 10). The notable deviation from elongation to failure may have been caused by unexpected defects during SLM fabrication. It is worth noting that the stress-strain curve of SLM parts does not exhibit a distinct stage of stress strengthening.

Further enhancement of the tensile strength of the 3D printed parts could be achieved through processes like isostatic pressure or additional heat treatments. Table 9 illustrates that rolled 316L stainless steel exhibits an elongation of 40 %, whereas 3D printed parts demonstrate an elongation ranging from 42 ± 1 % to 52 ± 1 %. Hence, the SLM process displays a greater degree of plasticity compared to the rolling process.

3.7. Fractography

As depicted in Fig. 11, fracture surfaces of SLM SS316L are presented at three different scanning speeds: 1100 mm/s, 1200 mm/s, and 1300 mm/s. The specimens shown in Fig. 11 (a), (b), and (c) exhibit characteristics of both ductile and brittle fractures.

Additionally, brittle fractures are discernible where melt pools have been pulled out alongside sub-micron-sized dimples, indicating ductile behavior. At a scanning speed of 1300 mm/s, the specimen demonstrates a more brittle behavior than the other specimens, as per the results of the tensile tests.

The fracture surfaces of the specimens reveal numerous crater-like pores, varying in size from tens of microns to 150 μm. These larger

voids are believed to contribute to material failure during tensile tests [68]. Fig. 11(d) highlights spherical powder granules (indicated by black arrows) that have not undergone melting within these voids. In certain instances, some powder particles may remain either unmelted or partially melted in non-overlapping areas when the melt pools do not coincide (as depicted in Fig. 11(e)).

Consequently, during tensile testing, these regions characterized by lower density and strength surrounding each melting pool are inclined to detach from the fracture surface, forming crater-like voids. While mitigating such defects by fine-tuning input scanning parameters might be feasible, eliminating them could be more challenging. Remarkably, the material's mechanical properties, including its Ultimate Tensile Strength (UTS), do not suffer adverse effects from these inevitable imperfections in SLM SS316L, such as regions with lower density. As a result, materials produced through SLM exhibit a notable resilience to defects [47,69]. Compared to previous experiments with austenitic steels, the ductile dimples observed in this study are notably more minor on average.

Fig. 11(f) reveals that the intragranular cell size primarily dictates the size of the dimples. These dimples range from a few hundred nanometers to a few microns, aligning closely with the intragranular cells. Cracks occur when micro-voids at defect sites, such as second-phase inclusions, coalesce during tensile tests. Due to the prevalent presence of cellular networks, only nano-voids can form in SLM SS316L. Consequently, fractures tend to transpire more ductility at nano-void necks than micro-void necks, forming nano-sized dimples on the fracture surfaces [70,71].

In summary, tensile fractures manifest in two distinct ways: The first is the junctions of layers; a fragile crack initiates and intensifies under tension. As stress concentrations trigger the crack's progression, it adopts a scallop pattern as it extends into the micro crack within, and the second is the fact that the crack continues until it encounters the unmelted metal powder, resulting in a smooth outer surface. Upon reaching a defect-free region, fluctuations in stress intensify, leading to plastic necking and the subsequent formation of a dimple. The propagation of cracks is contingent on various factors, including crack size and type, whether it encounters unmelted powder or defect-free areas, and more. The progression of cracks manifests a diverse array of tearing patterns, such as scallops, dimples, and smooth surfaces [32,68,72,73].

4. Conclusions

This study evaluated the impact of crucial SLM parameters on 316L hardness and density, specifically laser power, scanning speed, and hatch distance.

1. Ferrite phases were not detected in the powder, nor at the highest and lowest energy densities of 31 J/mm^3 and 156 J/mm^3.
2. With a laser power of 180 W, a scan speed of 1200 mm/s, and a layer thickness of 0.03 mm, the best results were achieved, which equated to an energy density of 125 J/mm^3. A peak density of 99.5 % and a hardness of 220 HV were obtained from this configuration.
3. As energy density was reduced, narrow and shallow melt pools resulted, as did unmelted powders with micro-cracks at the matrix interface. In contrast, the 125 J/mm^3 energy density produced large, deep melt pools without unmelted powders or cracks. Keyhole pores were formed as energy density increased.
4. The ANOVA results indicate that scanning speed is the most significant for affecting density, followed by layer thickness and power.
5. The porosity and microstructure of the as-built part have a major impact on its hardness. Scan speed is the most critical parameter affecting hardness, followed by power, while layer thickness is comparatively less important.
6. The yield and tensile strength of the parts range from 624 ± 8 MPa to 649 ± 4 MPa. The grain size and the defects directly affect these

values. Strength values drop as scanning speed increases and energy density decreases because of a decrease in material density.

Declaration of competing interest

The authors declare the following financial interests/personal relationships which may be considered as potential competing interests: Hamid Omidvar reports equipment, drugs, or supplies was provided by 2. Center for International Scientific Studies and Collaboration(CISSC). If there are other authors, they declare that they have no known competing financial interests or personal relationships that could have appeared to influence the work reported in this paper.

Acknowledgement

References

[1] Gatões D, Alves R, Alves B, Vieira MT. Selective laser melting and mechanical properties of stainless steels. Materials 2022;15:7575.

[2] Park S-H, Son S-J, Lee S-B, Yu J-H, Ahn S-J, Choi Y-S. Surface machining effect on material behavior of additive manufactured SUS 316L. J Mater Res Technol 2021;13:38–47. https://doi.org/10.1016/j.jmrt.2021.04.031.

[3] Zhou B, Xu P, Li W, Liang Y, Liang Y. Microstructure and anisotropy of the mechanical properties of 316L stainless steel fabricated by selective laser melting. Metals 2021;11:775.

[4] Zheng Q, sheng Chen H, Zhou J, Wang W, xiao Xi S, Yuan Y. Effect of boron element on microstructure and mechanical properties of 316L stainless steel manufactured by selective laser melting. J Mater Res Technol 2023;26:3744–55. https://doi.org/10.1016/j.jmrt.2023.08.148.

[5] Li Y, Ge Y, Lei J, Bai W. Mechanical properties and constitutive model of selective laser melting 316L stainless steel at different scanning speeds. Adv Mater Sci Eng 2022:2022.

[6] McCann R, Obeidi MA, Hughes C, McCarthy É, Egan DS, Vijayaraghavan RK, et al. In-situ sensing, process monitoring and machine control in Laser Powder Bed Fusion: a review. Addit Manuf 2021;45:102058.

[7] Gong G, Ye J, Chi Y, Zhao Z, Wang Z, Xia G, et al. Research status of laser additive manufacturing for metal: a review. J Mater Res Technol 2021;15:855–84.

[8] Pinomaa T, Lindroos M, Walbrühl M, Provatas N, Laukkanen A. The significance of spatial length scales and solute segregation in strengthening rapid solidification microstructures of 316L stainless steel. Acta Mater 2020;184:1–16.

[9] Bahl S, Mishra S, Yazar KU, Kola IR, Chatterjee K, Suwas S. Non-equilibrium microstructure, crystallographic texture and morphological texture synergistically result in unusual mechanical properties of 3D printed 316L stainless steel. Addit Manuf 2019;28:65–77.

[10] Bansal GK, Chandan AK, Srivastava VC, Krishna KG, Das G, Rajkumar S, et al. Studies on tensile behaviour of selective laser melted 316l stainless steel using SEM straining stage. Trans Indian Natl Acad Eng 2021;6:1005–15.

[11] Tucho WM, Lysne VH, Austbø H, Sjolyst-Kverneland A, Hansen V. Investigation of effects of process parameters on microstructure and hardness of SLM manufactured SS316L. J Alloys Compd 2018;740:910–25. https://doi.org/10.1016/j.jallcom.2018.01.098.

[12] Zhang Z, Chu B, Wang L, Lu Z. Comprehensive effects of placement orientation and scanning angle on mechanical properties and behavior of 316L stainless steel based on the selective laser melting process. J Alloys Compd 2019;791:166–75.

[13] Xiang H, Zhao W, Lu Y. Effect of solution temperature on microstructure and mechanical properties of selective laser melted Fe–22Cr–5Ni-0.26N duplex stainless steel. J Mater Res Technol 2022;19:1379–89. https://doi.org/10.1016/j.jmrt.2022.05.124.

[14] Sander G, Babu AP, Gao X, Jiang D, Birbilis N. On the effect of build orientation and residual stress on the corrosion of 316L stainless steel prepared by selective laser melting. Corrosion Sci 2021;179:109149. https://doi.org/10.1016/j.corsci.2020.109149.

[15] saxena P, Gajera H, Shah D, Pancholi N. Effect of SLM process parameters on hardness and microstructure of stainless steel 316 material. Mater Today Proc 2022;50:1653–9. https://doi.org/10.1016/j.matpr.2021.09.144.

[16] Tolosa I, Garciandía F, Zubiri F, Zapirain F, Esnaola A. Study of mechanical properties of AISI 316 stainless steel processed by "selective laser melting". following different manufacturing strategies. Int J Adv Manuf Technol 2010;51:639–47. https://doi.org/10.1007/s00170-010-2631-5.

[17] Kurzynowski T, Gruber K, Stopyra W, Kuźnicka B, Chlebus E. Correlation between process parameters, microstructure and properties of 316 L stainless steel processed by selective laser melting. Mater Sci Eng A 2018;718:64–73. https://doi.org/10.1016/j.msea.2018.01.103.

[18] Jeon JM, Park JM, Yu J-H, Kim JG, Seong Y, Park SH, et al. Effects of microstructure and internal defects on mechanical anisotropy and asymmetry of

selective laser-melted 316L austenitic stainless steel. Mater Sci Eng A 2019;763: 138152. https://doi.org/10.1016/j.msea.2019.138152.

[19] Jing G, Wang Z. Influence of molten pool mode on microstructure and mechanical properties of heterogeneously tempered 300M steel by selective laser melting. J Mater Process Technol 2021;296:117188.

[20] Gu H, Wei C, Li L, Han Q, Setchi R, Ryan M, et al. Multi-physics modelling of molten pool development and track formation in multi-track, multi-layer and multi-material selective laser melting. Int J Heat Mass Transf 2020;151:119458.

[21] Qiu Y-D, Wu J-M, Chen A-N, Chen P, Yang Y, Liu R-Z, et al. Balling phenomenon and cracks in alumina ceramics prepared by direct selective laser melting assisted with pressure treatment. Ceram Int 2020;46:13854–61.

[22] Boutaous M, Liu X, Siginer DA, Xin S. Balling phenomenon in metallic laser based 3D printing process. Int J Therm Sci 2021;167:107011.

[23] Ronneberg T, Davies CM, Hooper PA. Revealing relationships between porosity, microstructure and mechanical properties of laser powder bed fusion 316L stainless steel through heat treatment. Mater Des 2020;189:108481.

[24] Hirata T, Kimura T, Nakamoto T. Effects of hot isostatic pressing and internal porosity on the performance of selective laser melted AlSi10Mg alloys. Mater Sci Eng A 2020;772:138713.

[25] Sun Z, Tan X, Tor SB, Chua CK. Simultaneously enhanced strength and ductility for 3D-printed stainless steel 316L by selective laser melting. NPG Asia Mater 2018;10: 127–36.

[26] Khorasani AM, Gibson I, Ghaderi AR. Rheological characterization of process parameters influence on surface quality of Ti-6Al-4V parts manufactured by selective laser melting. Int J Adv Manuf Technol 2018;97:3761–75.

[27] Larimian T, AlMangour B, Grzesiak D, Walunj G, Borkar T. Effect of laser spot size, scanning strategy, scanning speed, and laser power on microstructure and mechanical behavior of 316L stainless steel fabricated via selective laser melting. J Mater Eng Perform 2022;31:2205–24.

[28] Hsu H-C, Wong K-K, Wu S-C, Hou P-J, Ho W-F. Microstructure and properties of 316L stainless steel by selective laser melting under various process parameters. MRS Commun 2022;12:768–72.

[29] Röttger A, Boes J, Theisen W, Thiele M, Esen C, Edelmann A, et al. Microstructure and mechanical properties of 316L austenitic stainless steel processed by different SLM devices. Int J Adv Manuf Technol 2020;108:769–83.

[30] Yoon KB, Dao VH, Yu JM. Effects of build direction on tensile and creep properties of 316L stainless steel produced by selective laser melting. Fatigue Fract Eng Mater Struct 2020;43:2623–36.

[31] Spierings AB, Schneider MU, Eggenberger R. Comparison of density measurement techniques for additive manufactured metallic parts. Rapid Prototyp. J. 2011;17: 380–6.

[32] Yadroitsev I, Yadroitsava I, Du Plessis A, MacDonald E. Fundamentals of laser powder bed fusion of metals. Elsevier; 2021.

[33] Greco S, Gutzeit K, Hotz H, Kirsch B, Aurich JC. Selective laser melting (SLM) of AISI 316L—impact of laser power, layer thickness, and hatch spacing on roughness, density, and microhardness at constant input energy density. Int J Adv Manuf Technol 2020;108:1551–62.

[34] Donik Č, Kraner J, Paulin I, Godec M. Influence of the energy density for selective laser melting on the microstructure and mechanical properties of stainless steel. Metals 2020;10:919.

[35] Ghayoor M, Lee K, He Y, Chang C, Paul BK, Pasebani S. Selective laser melting of 304L stainless steel: role of volumetric energy density on the microstructure, texture and mechanical properties. Addit Manuf 2020;32:101011.

[36] Wu H, Ren Y, Ren J, Liang L, Li R, Fang Q, et al. Selective laser melted AlSi10Mg alloy under melting mode transition: microstructure evolution, nanomechanical behaviors and tensile properties. J Alloys Compd 2021;873:159823.

[37] Lu J, Lin X, Kang N, Cao Y, Wang Q, Huang W. Keyhole mode induced simultaneous improvement in strength and ductility of Sc modified Al–Mn alloy manufactured by selective laser melting. Mater Sci Eng A 2021;811:141089.

[38] King WE, Barth HD, Castillo VM, Gallegos GF, Gibbs JW, Hahn DE, et al. Observation of keyhole-mode laser melting in laser powder-bed fusion additive manufacturing. J Mater Process Technol 2014;214:2915–25.

[39] Zhang X, Yocom CJ, Mao B, Liao Y. Microstructure evolution during selective laser melting of metallic materials: a review. J Laser Appl 2019;31:31201.

[40] Dutt AK, Bansal GK, Tripathy S, Gopala Krishna K, Srivastava VC, Ghosh Chowdhury S. Optimization of selective laser melting (SLM) additive manufacturing process parameters of 316L austenitic stainless steel. Trans Indian Inst Met 2023;76:335–45.

[41] Vafaei M, Mashhuriazar A, Omidvar H, Sajuri Z. In-service welding of X70 steel gas pipeline: numerical and experimental investigations. J Mater Res Technol 2023;26: 6907–18. https://doi.org/10.1016/j.jmrt.2023.09.006.

[42] Mashhuriazar A, Gur CH, Sajuri Z, Omidvar H. Effects of heat input on metallurgical behavior in HAZ of multi-pass and multi-layer welded IN-939 superalloy. J Mater Res Technol 2021;15:1590–603.

[43] Jiang H-Z, Li Z-Y, Feng T, Wu P-Y, Chen Q-S, Feng Y-L, et al. Factor analysis of selective laser melting process parameters with normalised quantities and Taguchi method. Opt Laser Technol 2019;119:105592.

[44] Wang D, Song C, Yang Y, Bai Y. Investigation of crystal growth mechanism during selective laser melting and mechanical property characterization of 316L stainless steel parts. Mater Des 2016;100:291–9.

[45] Liu S, Lee M, Choi C, Shin K. Effect of additive manufacturing of SUS316L using selective laser melting. J Mater Res Technol 2023;24:9824–33.

[46] Shifeng W, Shuai L, Qingsong W, Yan C, Sheng Z, Yusheng S. Effect of molten pool boundaries on the mechanical properties of selective laser melting parts. J Mater Process Technol 2014;214:2660–7. https://doi.org/10.1016/j.jmatprotec.2014.06.002.

[47] Zhong Y, Liu L, Wikman S, Cui D, Shen Z. Intragranular cellular segregation network structure strengthening 316L stainless steel prepared by selective laser melting. J Nucl Mater 2016;470:170–8. https://doi.org/10.1016/j.jnucmat.2015.12.034.

[48] Acevedo R, Sedlak P, Kolman R, Fredel M. Residual stress analysis of additive manufacturing of metallic parts using ultrasonic waves: state of the art review. J Mater Res Technol 2020;9:9457–77. https://doi.org/10.1016/j.jmrt.2020.05.092.

[49] Yakout M, Elbestawi MA, Veldhuis SC. Density and mechanical properties in selective laser melting of Invar 36 and stainless steel 316L. J Mater Process Technol 2019;266:397–420.

[50] Abd-Elaziem W, Elkatatny S, Abd-Elaziem A-E, Khedr M, Abd El-baky MA, Hassan MA, et al. On the current research progress of metallic materials fabricated by laser powder bed fusion process: a review. J Mater Res Technol 2022;20: 681–707. https://doi.org/10.1016/j.jmrt.2022.07.085.

[51] Sun J, Sun Q, Liu Y, Li B, Zhang Z, Xu B, et al. Improving corrosion resistance of selective laser melted 316L stainless steel through ultrasonic severe surface rolling. J Mater Res Technol 2022;20:4378–91. https://doi.org/10.1016/j.jmrt.2022.09.011.

[52] Huang M, Zhang Z, Chen P. Effect of selective laser melting process parameters on microstructure and mechanical properties of 316L stainless steel helical micro-diameter spring. Int J Adv Manuf Technol 2019;104:2117–31. https://doi.org/10.1007/s00170-019-03928-3.

[53] Larimian T, AlMangour B, Grzesiak D, Walunj G, Borkar T. Effect of laser spot size, scanning strategy, scanning speed, and laser power on microstructure and mechanical behavior of 316L stainless steel fabricated via selective laser melting. J Mater Eng Perform 2021:1–20.

[54] Han L, Wang Y, Liu S, Zhang Z, Song X, Li Y, et al. Effect of cryogenic treatment on the microstructure and mechanical properties of selected laser melted H13 steel. J Mater Res Technol 2022;21:5056–65.

[55] Birnbaum AJ, Steuben JC, Barrick EJ, Iliopoulos AP, Michopoulos JG. Intrinsic strain aging, Σ3 boundaries, and origins of cellular substructure in additively manufactured 316L. Addit Manuf 2019;29:100784.

[56] Prashanth KG, Eckert J. Formation of metastable cellular microstructures in selective laser melted alloys. J Alloys Compd 2017;707:27–34.

[57] Boes J, Röttger A, Becker L, Theisen W. Processing of gas-nitrided AISI 316L steel powder by laser powder bed fusion–Microstructure and properties. Addit Manuf 2019;30:100836.

[58] Li R, Shi Y, Wang Z, Wang L, Liu J, Jiang W. Densification behavior of gas and water atomized 316L stainless steel powder during selective laser melting. Appl Surf Sci 2010;256:4350–6.

[59] Gong H, Rafi K, Gu H, Starr T, Stucker B. Analysis of defect generation in Ti–6Al–4V parts made using powder bed fusion additive manufacturing processes. Addit Manuf 2014;1:87–98.

[60] Yang T, Mazumder S, Jin Y, Squires B, Sofield M, Pantawane MV, et al. A review of diagnostics methodologies for metal additive manufacturing processes and products. Materials 2021;14. https://doi.org/10.3390/ma14174929.

[61] Zhou X, Wang D, Liu X, Zhang D, Qu S, Ma J, et al. 3D-imaging of selective laser melting defects in a Co–Cr–Mo alloy by synchrotron radiation micro-CT. Acta Mater 2015;98:1–16.

[62] de Terris T, Andreau O, Peyre P, Adamski F, Koutiri I, Gorny C, et al. Optimization and comparison of porosity rate measurement methods of Selective Laser Melted metallic parts. Addit Manuf 2019;28:802–13. https://doi.org/10.1016/j.addma.2019.05.035.

[63] Hu Z, Nagarajan B, Song X, Huang R, Zhai W, Wei J. Formation of SS316L single tracks in micro selective laser melting: surface, geometry, and defects. Adv Mater Sci Eng 2019;2019:9451406. https://doi.org/10.1155/2019/9451406.

[64] Tran H-C, Lo Y-L, Le T-N, Lau AK-T, Lin H-Y. Multi-scale simulation approach for identifying optimal parameters for fabrication ofhigh-density Inconel 718 parts using selective laser melting. Rapid Prototyp J 2022;28:109–25. https://doi.org/10.1108/RPJ-11-2020-0278.

[65] Bruna-Rosso C, Demir AG, Previtali B. Selective laser melting finite element modeling: validation with high-speed imaging and lack of fusion defects prediction. Mater Des 2018;156:143–53. https://doi.org/10.1016/j.matdes.2018.06.037.

[66] Bang GB, Kim WR, Kim HK, Park H-K, Kim GH, Hyun S-K, et al. Effect of process parameters for selective laser melting with SUS316L on mechanical and microstructural properties with variation in chemical composition. Mater Des 2021;197:109221. https://doi.org/10.1016/j.matdes.2020.109221.

[67] Liu J, Song Y, Chen C, Wang X, Li H, Wang J, et al. Effect of scanning speed on the microstructure and mechanical behavior of 316L stainless steel fabricated by selective laser melting. Mater Des 2020;186:108355.

[68] Waqar S, Liu J, Sun Q, Guo K, Sun J. Effect of post-heat treatment cooling on microstructure and mechanical properties of selective laser melting manufactured austenitic 316L stainless steel. Rapid Prototyp. J. 2020;26:1739–49.

[69] Zhang B, Dembinski L, Coddet C. The study of the laser parameters and environment variables effect on mechanical properties of high compact parts elaborated by selective laser melting 316L powder. Mater Sci Eng A 2013;584: 21–31. https://doi.org/10.1016/j.msea.2013.06.055.

[70] Wood P, Libura T, Kowalewski ZL, Williams G, Serjouei A. Influences of horizontal and vertical build orientations and post-fabrication processes on the fatigue behavior of stainless steel 316L produced by selective laser melting. Materials 2019;12. https://doi.org/10.3390/ma12244203.

[71] Stoll P, Spierings A, Wegener K. Impact of a process interruption on tensile properties of SS 316L parts and hybrid parts produced with selective laser melting.

Int J Adv Manuf Technol 2019;103:367–76. https://doi.org/10.1007/s00170-019-03560-1.

[72] Montero Sistiaga M, Nardone S, Hautfenne C, Van Humbeeck J. Effect of heat treatment of 316L stainless steel produced by selective laser melting (SLM). Proc. 27th Annu. Int. Solid Free. Fabr. Symp. Addit. Manuf. Conf., Solid Freeform Fabrication 2016:558–65.

[73] Wang X, Sanchez-Mata O, Atabay SE, Muñiz-Lerma JA, Shandiz MA, Brochu M. Crystallographic orientation dependence of Charpy impact behaviours in stainless steel 316L fabricated by laser powder bed fusion. Addit Manuf 2021;46:102104.